



THE UNIVERSITY *of* EDINBURGH

Edinburgh Research Explorer

Three-dimensional solar evaporation enhancement by superhydrophilic copper foam inverted cone and graphene oxide functionalization synergistic cooperation

Citation for published version:

Lv, F, Miao, J, Hu, J & Orejon Mantecon, D 2023, 'Three-dimensional solar evaporation enhancement by superhydrophilic copper foam inverted cone and graphene oxide functionalization synergistic cooperation', *Small*. <https://doi.org/10.1002/smll.202208137>

Digital Object Identifier (DOI):

[10.1002/smll.202208137](https://doi.org/10.1002/smll.202208137)

Link:

[Link to publication record in Edinburgh Research Explorer](#)

Document Version:

Publisher's PDF, also known as Version of record

Published In:

Small

General rights

Copyright for the publications made accessible via the Edinburgh Research Explorer is retained by the author(s) and / or other copyright owners and it is a condition of accessing these publications that users recognise and abide by the legal requirements associated with these rights.

Take down policy

The University of Edinburgh has made every reasonable effort to ensure that Edinburgh Research Explorer content complies with UK legislation. If you believe that the public display of this file breaches copyright please contact openaccess@ed.ac.uk providing details, and we will remove access to the work immediately and investigate your claim.



3D Solar Evaporation Enhancement by Superhydrophilic Copper Foam Inverted Cone and Graphene Oxide Functionalization Synergistic Cooperation

Fengyong Lv,* Jie Miao, Jing Hu,* and Daniel Orejon*

Solar evaporation has become a promising and sustainable technique for harvesting freshwater from seawater and wastewater. However, the applicability and efficacy of solar evaporation need further improvement to achieve high production closer to theoretical limits in compact systems. A 3D (three-dimensional) hierarchical inverted conical solar evaporation is developed, which consists of a 3D copper foam skeleton cone decorated with micro-/nano-structures functionalized with graphene oxide, fabricated via easy and scalable wet oxidation, impregnation, and drying at room temperature. The proposed configuration empowers high-efficiency solar absorption, continuous liquid film spreading and transport, enhanced interfacial local evaporation, and rapid vapor diffusion through the pores. More notably, the 3D conical evaporator realizes thermal localization at the skeleton interface and allows evaporation to occur along the complete structure with unimpeded liquid and vapor rapid diffusion. The solar-thermal evaporation efficiency under 1-Sun is as high as 93% with a maximum evaporation rate per unit area of $1.71 \text{ kg}\cdot\text{m}^{-2}\cdot\text{h}^{-1}$. This work highlights the benefits of synergistic cooperation of an easily scalable 3D hierarchical functional micro-/nano-structured copper foam skeletons and functionalized graphene oxide for high-efficient solar evaporation of interest to numerous applications.

1. Introduction

Solving the increasingly serious worldwide shortage of freshwater is one of the great challenges facing mankind and a priority within the United Nation Sustainable Development Goals. To overcome such challenges, developing new methods for the harvesting of sustainable water resources by using non-polluting and renewable green clean energy, amongst others, is much needed.^[1] To this end, solar energy radiation has become the focus of attention because of its unique advantages of being cheap, accessible, pollution-free, and inexhaustible. By making use of solar energy from radiation it is possible to extract fresh water from brine and/or even from polluted water by driving the “clean” water away from the contaminated water via evaporation.^[2] The working principle of traditional solar volume evaporators is to directly irradiate with sunlight a large amount of water, which effect can

be enhanced by dispersing metal particles (with solar-thermal conversion effect) into water.^[3] Upon solar irradiation, vapor is generated at the air-water interface leading to inevitable heat losses due to evaporative cooling and others, which leads to low solar energy utilization. To avoid such losses, the concept of interfacial evaporation where absorbed solar energy is converted into heat easing the evaporation of the water wicking and spreading over the solar evaporator and away from the bulk has been put forward,^[4] which is regarded as the premises for the realization of thermal localization.^[5] Thermal localized desalination systems exploit the advantages of enhanced water thin film infiltration over the evaporator surface and the accurate solar energy localization empowering high thin film evaporation, accelerated vapor diffusion transport, and heat loss minimization.^[6] Currently, the theoretical production rate of fresh water on passive and portable solar evaporators ranges from 1 to $10 \text{ L}\cdot\text{m}^{-2}\cdot\text{h}^{-1}$ for basic and thermally localized ones, respectively, which are within the same orders of magnitude as operational limits but far from the thermodynamic limit of $\approx 100 \text{ L}\cdot\text{m}^{-2}\cdot\text{h}^{-1}$.^[6a]


In order to prompt solar evaporator efficiencies closer to their thermodynamic limit, the synergistic cooperation of advanced materials properties and structures plays a paramount role in the optimal design and maximization of solar interfacial

F. Lv, J. Miao
School of Urban Construction and Safety Engineering
Shanghai Institute of Technology
Shanghai 201418, China
E-mail: fengyonglv@alumni.sjtu.edu.cn

J. Hu
School of Perfume and Aroma Technology
Shanghai Institute of Technology
Shanghai 201418, China
E-mail: hujing616@126.com

D. Orejon
School of Engineering, Institute for Multiscale Thermofluids
The University of Edinburgh
Edinburgh, Scotland EH9 3FD, UK
E-mail: d.orejon@ed.ac.uk

D. Orejon
International Institute for Carbon-Neutral Energy Research (WPI-I2CNER)
Kyushu University
744 Motooka, Nishi-ku, Fukuoka 819-0395, Japan

 The ORCID identification number(s) for the author(s) of this article can be found under <https://doi.org/10.1002/smll.202208137>.

© 2023 The Authors. Small published by Wiley-VCH GmbH. This is an open access article under the terms of the Creative Commons Attribution License, which permits use, distribution and reproduction in any medium, provided the original work is properly cited.

DOI: 10.1002/smll.202208137

evaporation. The basic performance requirements of solar evaporators include high solar energy absorption, optimal solar-thermal evaporation efficiency, continuous and sufficient water transportation, unimpeded vapor diffusion mechanisms, and minimum heat loss.^[7] At present, limited production rates are owed to the inevitable heat loss caused by the high light reflectivity and thermal radiation in the case 2D (two-dimensional) plane evaporators, which have prompted the investigation and development of 3D (three-dimensional) volume structured evaporators.^[7b,8] By employing unique 3D structures, the amount of light absorbed as well as the different pathways for water transport and vapor diffusion can be enhanced and/or tailored to our advantage.^[9] To this end, a macroscale 3D cup-shape solar evaporator was designed by Shi et al., which can recover most of the energy loss in a 2D plane photothermal material by capturing the multiple diffuse reflections of sunlight within the cup-shaped structure, leading to a high energy efficiency beyond 100%.^[10] Nonetheless, the introduction of a 3D structure only provided 16% to 18% higher evaporation rates per unit of area when compared to the 2D one, with a maximum of $1.46 \text{ kg} \cdot \text{m}^{-2} \cdot \text{h}^{-1}$. More recently, a 3D sunflower-shape photothermal evaporator was reported by Sun et al.^[11] The unique cavity shape of the sunflower allows for reabsorbing the energy lost by diffuse reflection and thermal radiation yielding evaporation rates of $1.51 \text{ kg} \cdot \text{m}^{-2} \cdot \text{h}^{-1}$ and a solar efficiency of 100.4% under 1-Sun illumination.^[11] More recently, a hierarchical porous carbonized lotus seedpods-shape evaporator was proposed by Fang et al. with excellent light absorption and photothermal conversion performance attributed to the conical lotus macrostructure coupled with the sunken structure of the cylindrical holes in the lotus.^[12] It is worth considering that in addition to the contribution of the macrostructures to light capture, microstructures also anticipate great potential for light reabsorption. The utilization of porous materials such as foams and thin films is a critical factor in solar interfacial evaporation, because these empower the light trapping effect by increasing the number of diffuse reflections through the light.^[12] In addition, the internal structure of porous materials such as hydrophilic hierarchical metal foams also maximizes the water transport toward the interface and the occurrence of confined phase-change.^[13]

Besides enhancing light absorption, managing efficiently both water transport and vapor diffusion mechanisms at the water-air interface is also an important step to be able to meet the global demand for water and thermal management.^[14] When looking into the liquid transport from the bulk to the photothermal conversion layer, the size scale plays a big role. Interconnected porous networks, bionic plant cells with directional water delivery capacity,^[11,15] and fiber structures inducing capillary effect,^[16] can all enhance liquid transport as well as the realization of interfacial evaporation. For instance, a coupled 2D-3D spiral-shaped evaporator with an increased area for evaporation and diffusion of the vapor from both the upper and lower surfaces of the evaporator with the consequently enhanced vapor generation efficiency has been proposed by Wang et al.^[17] More recently, Zhang et al. proposed a high efficient salt-rejecting evaporator by making use of a wick-free confined water layer achieving high evaporation rates per unit of area of $1.36 \text{ L} \cdot \text{m}^{-2} \cdot \text{h}^{-1}$ with a solar-to-vapor conversion

efficiency of 91% under 1-Sun illumination.^[18] However, poor water transport along the unconventional structure^[19] and heat losses caused by the direct contact of the wick-free water layer and the evaporator are some of the drawbacks, which call for further improvement.

Another approach to increase the water production rates is the use of carbon-based light-absorbing materials, which have only been briefly investigated in the field of solar evaporation. For instance, polypyrrole organic polymer coating deposited on or impregnated within the structured melamine foam aerogel^[20] with the upper surface of the melamine foam aerogel covered by a graphene oxide film has been investigated.^[21] However, the use of a polymer organic coating coupled with the foam aerogel yields a rather poor thermal conductivity. The low thermal conductivity can on the other hand be overcome by making use of the outstanding thermal conductivity of metal foams allowing the heat to spread more evenly. Within carbon-based materials, graphene has received increasing attention for the development of light-absorbing materials in recent years because of its high solar/light absorption and high thermal conductivity. Moreover, its optical and hydrophilic properties can be tailored to our advantage by adjusting its oxidation degree. For instance, the vapor generation efficiency of carbon black, graphitized carbon black, and graphene nanofluids under 10-Sun irradiation was reported as high as 69% additionally showing that the performance of transient and steady states could be significantly improved.^[22] More recently, Zhang et al. exploited both the photothermal conductivity and self-supporting channel water transport of functionalized vertically aligned graphene sheets membranes realizing an excellent evaporation rate per unit of area of $1.62 \text{ kg} \cdot \text{m}^{-2} \cdot \text{h}^{-1}$ with a photothermal conversion efficiency of 86.5%.^[23] Since then, a variety of graphene derivatives such as graphene oxide (GO), chemically reduced graphene oxide, functionalized chemically reduced graphene oxide, have been proposed to contribute to enhanced solar evaporation. However, optimizing and maximizing light absorption and hydrophilic properties of GO merits further investigation. Compared with the combination of nickel foam and graphene oxide,^[24] the pristine copper foam (PCF) coupled with GO offers enhanced thermal conductivity, so that the areas of the conical evaporator that are not directly irradiated by the sun can also be efficiently heated, which is also the key factor to achieve local thermal positioning.

Although macroscale 3D evaporators can compensate for some shortcomings originating from the 2D structure, there are still some limitations to be addressed. To overcome such limitations as well as to maximize the water production rate; in the present study, we introduce a 3D inverted conical solar evaporator (concave shape as in concentrated solar power) consisting of a 3D matrix material of hierarchical superhydrophilic (SHi) copper foam (CF) (SHiCF) and graphene oxide (GO). The advantages of our proposed system are the synergistic cooperation of enhanced water wicking transport and high light absorption through the porous SHiCF skeleton; enhanced area for the diffusion and transport of the vapor owed to its 3D structure;^[25] and further enhanced solar absorption and high water sorption rates owed to both the hierarchical SHiCF and the GO advanced functionalization.^[23] Moreover, the presence of an air-laid paper wrapping the macroscale evaporator also ease capillary wicking

from the bulk water to the skeleton of the evaporator and diffusion of the vapor from the SHiCF skeleton to the pores of the air-laid paper without obstruction instead of being trapped inside the CF pores. The adopted configuration provides a maximum evaporation rate per unit of area of $1.71 \text{ kg} \cdot \text{m}^{-2} \cdot \text{h}^{-1}$ is achieved, which is an 8% to 20% enhancement under 1-Sun radiation when compared to other recent works.^[18,11] Furthermore, the use of a polyethylene foam isolating the bulk water from the evaporator interface reduces heat losses via conduction down to a minimum of 0.6%, which is only 1/6 of the conduction heat loss of a sandwiched photothermal membrane.^[4] To sum up, the proposed design is able to achieve high efficient solar absorption, continuous and high water transport, and unimpeded vapor diffusion, providing relevant enhancements on evaporation rates with an easier and scalable fabrication procedure, with the consequent solar evaporator higher efficiency as well as minimum heat losses.

2. Result and Discussion

2.1. Solar Evaporator Surface Characterization

Schematics of the sunlight absorption proposed principle within the 3D inverted conical solar evaporator consisting of a 3D matrix material of hierarchical superhydrophilic copper foam (SHiCF) functionalized with graphene oxide (GO) is included in **Figure 1a**. While schematics of the 3D inverted conical solar evaporator wrapped in an air-laid paper including the polyethylene foam and air insulating layer between the evaporator and the bulk water, are presented in **Figure 1b**. The conical surface of the evaporator was created by bending the honeycomb type pristine copper foam (PCF) in a conical shape, and it was further chemically etched to create a uniform layer of copper oxide blade-like superhydrophilic nanostructures decorating the micro-structured skeleton of the CF as represented in **Figure 1c**. The 3D inverted conical solar evaporator with a cone's apex angle of 45° provides an enhanced projected area for the light incidence while maintaining a reasonable height for the water transport toward the top of the cone.^[3a] The implementation of the nano-structures modifies the chemical and physical properties of the foam inducing its superhydrophilic wetting behavior,^[26] henceforth referred to as SHiCF. It is worth noting that the PCF can be easily bent and folded into almost any 3D desired configuration maintaining its structure and shape under water load even after hours or days of operation, while the inner microscale pores act as optical traps allowing the repeated absorption of a large amount of reflected light experiencing multiple diffuse reflections along the cone matrix.^[27] Scanning electron microscopy (SEM) ZEISS Ultra Plus (Germany) snapshot of the SHiCF in **Figure 1d** shows the unique skeleton structure with pores in the micro-meter range decorated with nano-meter blades with thickness in the order of tens to a hundred nanometers and a few micrometers in length. The unique structure of the SHiCF allows for a sufficient path for light capture as well as enhanced water transport and vapor diffusion. While the dimensions of the pores are within 100–300 μm in diameter and $\approx 100 \mu\text{m}$ thickness of the copper network.^[28] The blackish termination of the SHiCF

micro- and/or nano- structures obtained by chemical etching has a significant impact on improving the hydrophilicity of the evaporating interface.^[29] In addition, subsequent GO impregnation introduces further oxygen containing polar groups such as carboxyl ($-\text{COOH}$) and hydroxyl groups ($-\text{OH}$), which in turn enhance water spreading and transport at the evaporation interface.^[30] The benefit of enhancing light absorption via reduced GO (RGO) is actually overcome by the better affinity of GO to water and to water transport exploited in this work. The chemical etching modifies the physicochemical properties of the CF by introducing hydrophilic groups that empower wetting while at the same time increasing the surface roughness leading to the superhydrophilicity of the SHiCF and the complete water droplet spreading with contact angles $\approx 0^\circ$ as shown in the inset in **Figure 1c**.^[30a,b,31] Thereafter, the SHiCF surface is functionalized with GO to form the SHiCF-GO, which also exhibits complete wetting upon droplet deposition. The abundant oxygen functional groups such as hydroxyl ($-\text{OH}$) and carboxyl ($-\text{COOH}$) groups attached to the GO molecular layer additionally empower excellent water sorption contributing further to the water transport capacity of the evaporator.^[23] SEM of SHiCF-GO-2.5 in **Figure 1e**^[31] (where 2.5 refers to the amount of GO solution in mg mL^{-1}) shows that by making use of an appropriate amount of GO below 3 mg mL^{-1} , upon impregnation, the GO interlocks within the skeleton structures by depositing evenly around and within the nanostructures of the micro-structured skeleton. Whereas for concentrations equal or above 3 mg mL^{-1} as for SHiCF-GO-3.0 in **Figure 1f**, the size of the pores decreases considerably clogged by the excess of GO leading to pore filling, which eventually inhibits transport and/or vapor diffusion, with the consequent lower evaporation rates reported. Physical SEM characterization clearly shows the absence of GO in SHiCF in **Figure 1d** when compared to SHiCF-GO-2.5 after impregnation provided in **Figure 1e** where the presence of GO locked within the micro-structures is clear. When looking into the stability of the GO, long-run experimental observations of up to 9 h showed no degradation of the evaporation performance/rate for any of the SHiCF-GO configurations studied, which means that GO is stable and not easy to be removed. **Figure S10**, Supporting Information shows up to 9 h of the SHiCF-GO-2.5 sample immersed in deionized water without any degradation or GO transfer to the bulk water.

On other hand, SHiCF and SHiCF-GO-2.5 functional group changes were studied via Fourier Transformed Infrared (FTIR) spectroscopy as shown in **Figure 1g** and **Figure S4c**, Supporting Information. FTIR spectrum for SHiCF-GO-2.5 in **Figure 1g** shows different peaks with centers at 1257, 1731, and 3602 cm^{-1} corresponding to C–O–C, C=O, and C–OH bonds, respectively, which prove the existence of a large number of oxygen-containing functional groups.^[32] While FTIR spectrum for SHiCF in **Figure S4c**, Supporting Information, shows clear differences in the arbitrary transmittance of the C–O–C peak at 1257 cm^{-1} , indicating that more light is reflected back with the consequent poorer light absorption in the absence of GO. Moreover, Raman spectrum of the stretching frequency of the O–H bonds for SHiCF-GO-2.5 in the presence of water infiltration is shown in **Figure 1h**. Four peaks are fitted by a Gaussian function revealing the state of different types of water molecules within the SHiCF-GO-2.5 infiltrated solar evaporator. The

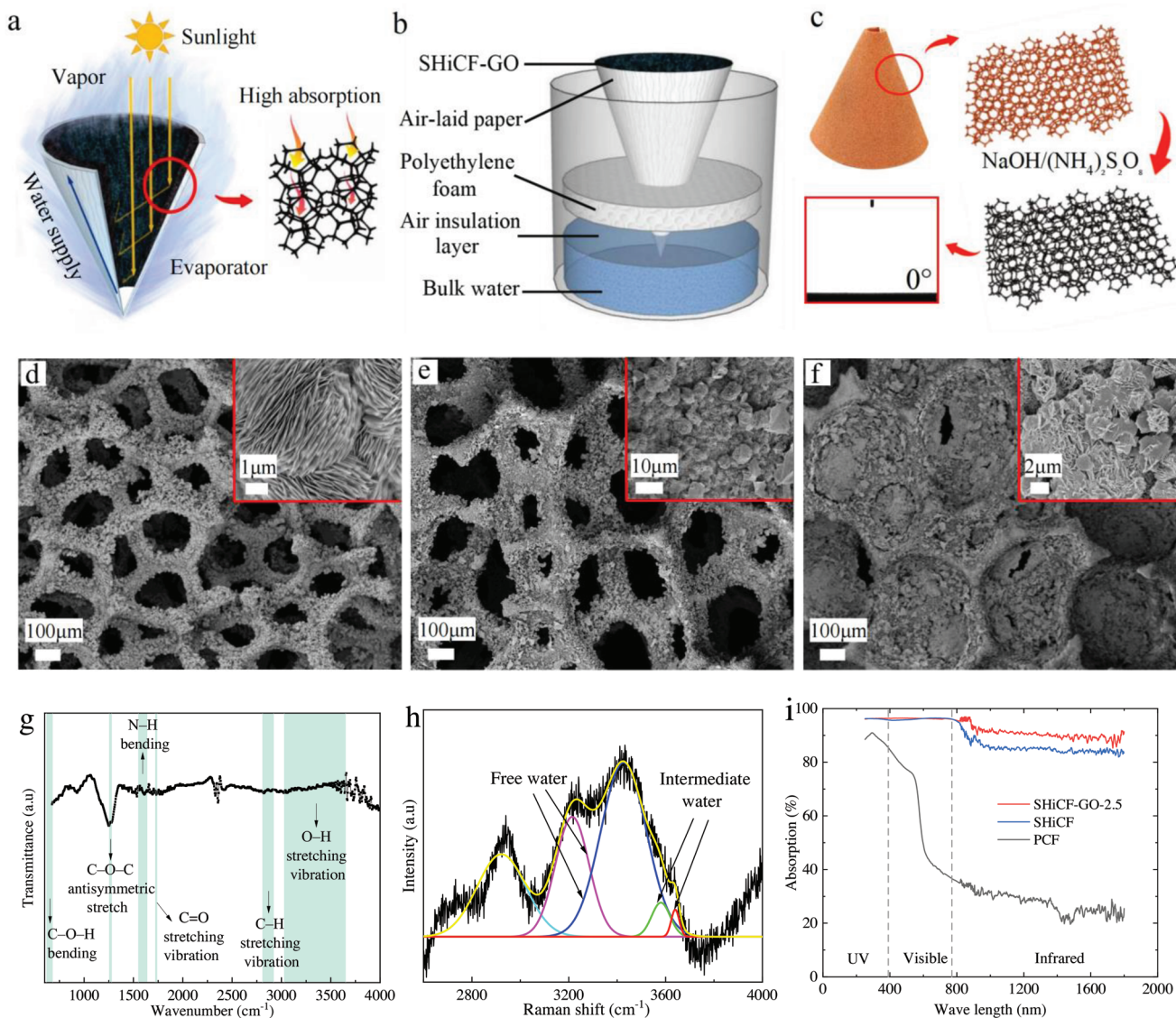


Figure 1. Schematics of the proposed light absorption principle, evaporator, fabrication process, and characterization of the 3D inverted conical solar evaporator. a) Schematic illustration of the proposed solar evaporator and light absorption principle. b) Schematic illustration of the solar evaporator apparatus with a thermally insulating layer. c) Functionalization process of the pristine copper foam (PCF) by chemical reaction with sodium hydroxide (NaOH) and ammonium persulfate ($(\text{NH}_4)_2\text{S}_2\text{O}_8$) inducing the formation of superhydrophilic nanostructures, which can be proved by water contact angle on the SHiCF surface. d) SEM images of SHiCF showing highly porous micro-structures and the blade-like nano-structures. e) SEM images of SHiCF coated with graphene oxide (SHiCF-GO-2.5). f) SEM images of SHiCF coated with graphene oxide (SHiCF-GO-3.0). g) FTIR spectra of SHiCF-GO-2.5. h) Raman spectrum of SHiCF-GO-2.5 showing the intensity of intermediate water (green and red) and free water (purple and blue). i) Absorbance spectra (%) of PCF, SHiCF, and SHiCF-GO surfaces in the wavelength range of ultraviolet light, visible light, and infrared rays, that is, from 250 to 1800 nm.

peaks at 3214 and at 3426 cm^{-1} correspond to the $-\text{OH}$ expansion and tetrahedral structure of free water, while the peaks at 3580 and at 3639 cm^{-1} are related to the weak hydrogen bond of intermediate water, showing a non-tetrahedral structure, which is conducive to the phase change of water and the diffusion of vapor.^[33] When directly comparing the Raman spectrum for SHiCF shown in Figure S4d, Supporting Information and that of SHiCF-GO-2.5 in Figure 1h, it is demonstrated that the content of intermediate water present in the SHiCF-GO-2.5 is relatively higher, which proves the presence of GO on how GO increases the proportion of intermediate water on the surface

facilitating water transport and evaporation. Both FTIR and Raman spectrum characterization supports well the presence of GO within the SHiCF-GO samples and the benefits of GO to facilitate water transport and evaporation.

For efficient solar evaporation, advanced functional materials that can adsorb light across the broadest range of the solar spectrum are a prerequisite, for which carbon-based materials are promising toward achieving this goal.^[34] As such carbon-based materials play a paramount role in improving the efficiency and water rate production in thermal localization systems. This is mainly owed to the following advantages: easy modification,

strong plasticity, and high light absorption efficiency.^[21,35] Compared with traditional carbon-based materials, GO has very low emissivity while ensuring high solar absorption.^[23] The absorption rates of PCF, SHiCF, and SHiCF-GO samples are measured using an ultraviolet-visible-near infrared (UV-VIS-NIR) spectrophotometer Shimadzu UV-3600 (Japan) and the corresponding results are shown in Figure 1i. The surface absorption rate is calculated by the weighted average absorptivity over the range of 250 to 2500 nm wavelength. The weighted average absorption rate for the SHiCF surface improves considerably when compared to the PCF surface owed to the presence of additional nano-structures increasing the surface area and the number of diffuse reflections when compared to the pristine one, which are 91.2% and 34.4% respectively. While the light absorption performance of SHiCF-GO-2.5 evaporator shows the best results with an average of 93.6%. Impregnating the SHiCF in a solution with higher or lower GO concentration shows a 2% decrease in the light absorption rate for both SHiCF-GO-2.0 and SHiCF-GO-3.0 down to 91.8 and 91.6% respectively, while the reflectivity for the SHiCF-GO-3.0 evaporator is also increased by 2% to 8.4% suggesting that higher GO blocks the pores and weakens the light trap effect leading to inhibition of light absorption. Evidences on the greater amount of GO impregnated within the pores of the SHiCF-GO-3.0 skeleton when compared to SHiCF-GO-2.5 can be retrieved from Figure 1f,e, respectively. See Table S1, Supporting Information for the different absorptivity, reflectivity, and transmissivity values for the different studied configurations.

The transmission rate of SHiCF and that of SHiCF-GO-2.5 measured using the same Ultraviolet-Visible-Near Infrared spectrophotometer are 0.2%, and 0.1% respectively as shown in Table S1, Supporting Information, which are rather negligible indicating that the incident solar energy/heat loss is mainly due to the reflection of light.^[21,36] While the introduction of nano-structures improves the absorptivity, the deposition of GO in SHiCF-GO; on the other hand, these reduce greatly the amount of reflected light with an average reflection rate of 6.3% for the solar wavelength range measured, which is lower than on the PCF and the SHiCF evaporators, measured as 56.0% and 8.6% respectively (Table S1, Supporting Information). The black nano-rough appearance of the SHiCF and SHiCF-GO surfaces is the reason for the excellent enhancements of the solar energy absorptive capacity. When the light is irradiated to the rough skeleton, there will be many irregular diffuse reflections between uneven micro-scale spherical-like structures and the nano-blade-like structures, so that most/all the light is absorbed with the consequent reduction on the total amount of reflected light. On the other hand, differing from conventional carbon materials, in the case of graphene and graphene oxide there is a shift of the infrared absorption light spectrum resulting from the increased conjugated π bonds in graphene, which greatly benefits the absorption of incident light.^[37] The shift of the absorption peak toward the infrared spectrum plays a key role in avoiding the ineffective utilization of solar energy due to infrared light dissipation into waste heat, which is the reason why materials that can absorb the full spectrum of the solar energy should be targeted.^[38] Efficient broadband solar light absorption corresponds to $\pi-\pi^*$ (C=C) transition and $n-\pi^*$ (C=O) transition.^[30b,39] The great increase in surface

absorbance achieved by the morphology and chemical properties of the copper micro- and nano-structures coupled with the presence of GO anticipate that superhydrophilic treatment and precipitation of GO are both essential steps for high efficient solar evaporator design and optimization. Moreover, the presence of water wicking through the solar absorber results in a further decrease of the surface reflectivity making the wet evaporator to have a better light absorption capacity than the dry surface.^[40] We note here that the light intensity emitted by the light source gradually decreases with the increase of the distance from the top to the bottom of the 3D conical evaporator. The incident light intensity at any height inside the conical evaporator can be obtained by fitting the solar radiation intensity at the bottom, middle, and top of the conical evaporator where I refers to the intensity of the incident light inside the conical evaporator after fitting, which decays as the distance from the light source increases, as shown in Figure S4b, Supporting Information. The empirical fitting for the intensity obeys the linear relation: $I = -5.66h + 170.81$.

2.2. Liquid and Vapor Transport Solar Evaporator Characteristics

The 3D conical solar evaporator composed of an air-laid paper and SHiCF or SHiCF-GO skeleton not only ensures that most of the sunlight reaching the pores is absorbed, but also provides the paths for water transport and vapor diffusion.^[39,41] The air-laid paper composed of cellulose and polyester is used as passive water transportation path easing water liquid molecules to continuously diffuse toward the SHiCF or the SHiCF-GO skeleton and then toward its interface in order to replenish the evaporating water.^[42]

The dense micro- and nano-structured framework of the CF also provides an efficient path for water capillary wicking and transport empowered by the increased roughness and superhydrophilic wettability, that is, SHiCF.^[39] The efficient and continuous capillary action ensures that the evaporating interface is continuously replenished and wetted during the process. Moreover, the high surface area of the skeleton structure provides enough space for the vapor diffusion from the interface toward the ambient. The synergistic cooperation of the superhydrophilic skeleton and air-laid paper prevents both the insufficient evaporation caused by untimely water supplement as well as heat loss caused by excessive water evaporation. In the present case, evaporation and diffusion of the vapor occur from both the air-laid paper and from the SHiCF skeleton toward the ambient realizing 3D interfacial evaporation. The exploitation of the synergistic cooperation of the porous CF and GO utilized in our work enhances water transport along the interface, vapor diffusion within the pores and as such provides higher evaporation rates than earlier evaporators such as the carbon fiber cone^[43] and the acrylonitrile-styrene-acrylate (ASA) cone.^[3a]

In order to measure the wettability and permeability of the PCF, SHiCF, and SHiCF-GO, capillary rise characterization experiments are conducted on the different surfaces at an inclination angle of 67.5° with respect to the horizontal (Figure 2a).^[44] The PCF sample decorated with rather large micro-pores in the absence of nano-structures presents difficulty toward wetting because of its poor wicking or capillary action force, which is

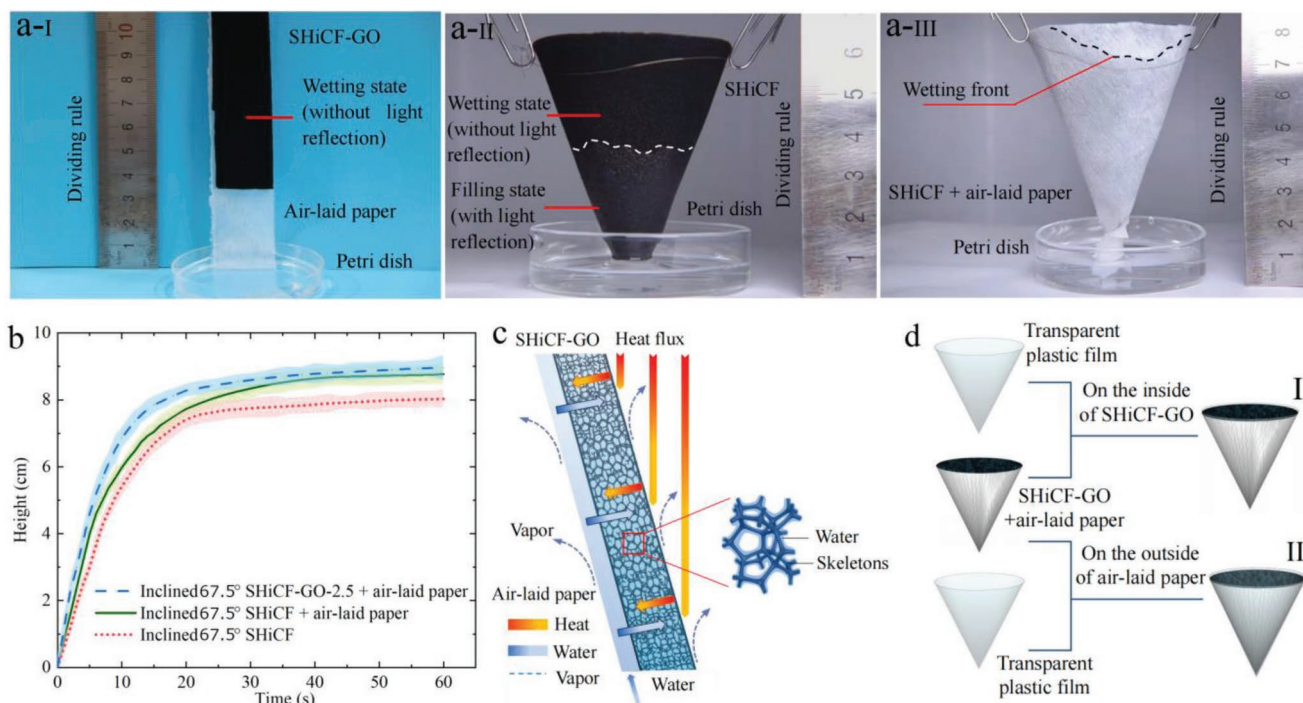


Figure 2. Capillary rise characterization. a) Snapshot of the capillary rise characterization for inclined aI) SHiCF-GO, aII) SHiCF evaporator, and aIII) SHiCF wrapped with air-laid paper evaporator before fully wetting the evaporator. b) Representative data of the measured capillary rise height (cm) as a function of time (s). The average and standard deviation represented have been obtained from two independent experiments. c) Schematics of the synergistic regulation of heat and mass water transport and vapor diffusion. d) Schematic illustration of solar evaporator whose I) inner and II) outer surfaces are covered by a transparent plastic film, forcing vapor to diffuse from one side of CF skeleton.

not large enough to overcome gravity. In contrast to the PCF sample, on the SHiCF (Figure S5, Supporting Information) the water rising wetting front follows a rather fast initial wicking and spreading behavior, followed by the gradual slowdown of the wetting front until it finally reaches equilibrium. Similar to the SHiCF sample, the wetting front on the SHiCF sample tightly wrapped with air-laid paper shows a similar qualitative trend to that reported for the SHiCF. However, the wicking process of the SHiCF and air-laid paper raises initially quicker and continues to rise for a longer time, indicating its excellent superhydrophilicity and wicking capabilities owing to the synergistic cooperation of the water transport through the air-laid paper as well as through the SHiCF, (Figure 2b) with a much better water transport than on sole SHiCF.^[45] The SHiCF and air-laid paper realizes the joint action of double path water transport, which are along the SHiCF plane, that is, along the cone edge, as well as through the SHiCF thickness, that is, from the air-laid paper-SHiCF interface toward the SHiCF-air interface.

When looking into the rising velocity and the final height of the water wetting front for SHiCF-GO sample, there is a slight increase when compared to the SHiCF sample, which is explained by the enhanced superhydrophilicity and water affinity to both the oxygen-containing groups and hydroxyl groups of the GO.^[26,31,46] The wetting front of water raising along the evaporator shows a similar phenomenon than for stripe capillary rise experiments. Figure 2a-II,III shows experimental snapshots and representation of the wetting front before reaching the top corresponding to experimental observations reported in Videos S1 and S2, Supporting Information

respectively. The direct contact between the SHiCF evaporator and the bulk water represented in Figure 2a-II makes the water to fully wick and spread from the bottom of the SHiCF interface, which results in light reflection, while the upper part of SHiCF presents a more moisty state rather than wetting state, which hinders light reflection. Water is continuously transported and confined along the SHiCF skeleton interface, rather than filled within the interconnection pores. Therefore, a water layer is formed around the CF skeleton, which can not only prevent the solar energy from heating the excess water, but also exposes as much evaporation area as possible to increase the path for vapor diffusion.^[47] Capillary raise experiments on custom-made stripes showing a final height of ≈ 8 cm ensure that the solar evaporator studied here of 5.5 cm in height is fully wetted by the transported water molecules from the water bulk to the top.

In the solar evaporation experiments, the SHiCF-GO is tightly adhered to the air-laid paper, which is in turn in direct contact with the bulk water. Hence, the SHiCF-GO outermost interface is just wetted by the water absorbed from the air-laid paper forming a water layer over the GO instead of at the SHiCF-GO interface, which ensures that the surface morphologies and chemical properties of the solar evaporator and those of the SHiCF-GO interface remain unchanged.^[47] Within 9 h of a solar evaporation experiment, the evaporation interface remains wet as a consequence of the excellent water absorption and transport characteristics owed to the synergistic cooperation of SHiCF-GO continuously wetted by the air-laid paper. As water turns into vapor, water molecules wick upward

and toward the evaporating interface along the superhydrophilic skeletons of the SHiCF-GO filling the nanoscale vacancies between the blade-like nanostructures around the skeleton (Figure 2c). Unlike ordinary solar evaporators where the vapor diffusion mechanism occurs from the interface of the water bulk toward the air, in the presence of thermally localized evaporation within our 3D conical evaporator, the vapor diffusion mechanism follows two distinctive vapor diffusion paths, namely the outside surface of the air-laid paper and the interconnected pores of the SHiCF-GO (Figure 2c). The stacked skeleton of the CF provides a path for the vapor diffusion via the different adjacent interconnected pores. When looking at the system in terms of energy and heat transfer, upon the incidence of the simulated sunlight at 1-Sun, the incident light is converted into heat by solar–thermal conversion. Heat is then absorbed by the SHiCF-GO and conducted across the CF toward the air-laid paper-SHiCF-GO interface and toward air-laid paper-air interface. Water infiltrated within the nanoscale pores between the blade-like structures of the SHiCF-GO and the air-laid paper then heats up generating water vapor. The vapor then diffuses through the pores from the inner wall of the SHiCF-GO toward the ambient as well as from the air-laid paper toward the ambient, in both parallel and normal directions to the SHiCF-GO skeleton as in Figure 2c.

In order to quantify the different contributions of the different layers and the presence of the double-layer interface composed by the SHiCF-GO and the air-laid paper, a thin transparent film is used to block the different vapor diffusion paths. On one hand, the contribution to the vapor diffusion toward the inner surface is estimated by wrapping the air-laid paper with the thin transparent plastic film so to block the vapor diffusion path through the outside plane (Figure 2d). Therefore, the vapor generated at the two evaporation interfaces of the air-laid paper and the SHiCF-GO skeletons can only diffuse toward the internal interconnected pores of the SHiCF-GO and the upper side surface of the 3D inverted cone evaporator. Under 1-Sun irradiation, a $1.25 \text{ kg} \cdot \text{m}^{-2} \cdot \text{h}^{-1}$ evaporation rate per unit of area, henceforth referred to as evaporation rate, is reported compared to $1.71 \text{ kg} \cdot \text{m}^{-2} \cdot \text{h}^{-1}$ for unrestricted vapor diffusion (Figure 3c), which indicates that $0.46 \text{ kg} \cdot \text{m}^{-2} \cdot \text{h}^{-1}$ of vapor cannot be efficiently diffused and evaporated if the vapor diffusion through the air-laid paper is hindered. This highlights the importance of water transport and evaporation through the air-laid paper enhancing the vapor diffusion path to ensure efficient solar evaporation. On the other hand, when the inner surface of the evaporator is blocked by the transparent plastic film, that is, the vapor diffusion path through the upper-inner part of the evaporator is blocked, the vapor generated from both the air-laid paper and the SHiCF-GO skeleton is forced to diffuse through the air-laid paper path. In this case, $0.71 \text{ kg} \cdot \text{m}^{-2} \cdot \text{h}^{-1}$ of water evaporates, which is $0.54 \text{ kg} \cdot \text{m}^{-2} \cdot \text{h}^{-1}$ lower than that of vapor only diffusing from the SHiCF-GO side. The low evaporation rate reported here is attributed to the increase in the path distance for the vapor diffusion along the SHiCF-GO, which additionally increases the diffusion resistance. Both effects combined have a weakening effect on evaporation. It can be concluded that the SHiCF-GO pore path makes a greater contribution to vapor diffusion than the air-laid paper path. The proposed design having two different main paths for vapor diffusion further promotes

evaporation; however, it needs to be considered that if the amount of vapor is rather large, vapor diffusion becomes then the limiting mechanism governing the efficiency of the solar evaporator and other additional techniques such as forced air-flow convection may be explored. Specific details on the calculations of the evaporation rate per unit of area follow the same procedure as reported in Cao et al.^[3a] and can be found in the accompanying Supporting Information.

2.3. Solar Evaporator Efficiency

When the sunlight is irradiated to the inner surface of the 3D conical evaporator, part of the light is absorbed and part of it is reflected and then absorbed multiple times owing to the concave shape of the cone that reflects the light toward the inner surface of the cone. Hence, the amount of reflected light to the surrounding environment is minimized and so are the heat losses.

Besides the contribution of the macroscopic concave shape of the cone to light absorption, the porous hierarchical structure of SHiCF additionally allows for multiple reflections within the pores enhancing light and energy absorbance efficiency.^[42a,48] When the incident light irradiates the hierarchical skeleton of the SHiCF-GO, there are many irregular diffusive reflections between the uneven spherical-like and honeycomb-like micro-scale structures decorated with nanoscale blade-like structures, so that the light is further absorbed multiple times by the dense blades and onto the globular structures. This phenomenon is called light trapping, which eventually reduces greatly the total amount of reflected light back to the environment. Under the synergistic cooperation of the conical volume structure, the porous CF frame structure, the hierarchical etched micro- and nano-structures, and the GO, the absorptivity of the evaporator is enhanced significantly to 93.6% (Table S1, Supporting Information). Thermal localization is then achieved uniformly at the evaporator's interface of the CF skeleton enabled by the high thermal conductivity of the CF, which allows evaporation to occur along the complete steric structure.

We now estimate the different contributions to evaporation for the different configurations tested without the addition of GO. It is worth noting that the light intensity emitted from the light source gradually weakens with the increase of distance from the upper part to the lower part of 3D conical evaporator as it was represented in Figure S4b, Supporting Information. With the help of a fitting formula, the light intensity attenuation with the increase of distance can be estimated. On one hand, at 1-Sun intensity the evaporation rates per projected area of the evaporator for air-laid paper, SHiCF, PCF-air-laid paper, and SHiCF-air-laid paper are measured as $0.60 \text{ kg} \cdot \text{m}^{-2} \cdot \text{h}^{-1}$, $1.06 \text{ kg} \cdot \text{m}^{-2} \cdot \text{h}^{-1}$, $1.19 \text{ kg} \cdot \text{m}^{-2} \cdot \text{h}^{-1}$, and $1.38 \text{ kg} \cdot \text{m}^{-2} \cdot \text{h}^{-1}$, respectively. While $0.12 \text{ kg} \cdot \text{m}^{-2} \cdot \text{h}^{-1}$ is obtained for pure water without any solar evaporator (Figure 3b), which is consistent and in agreement with literature refs. [3a,4,10] indicating the validity of the results.^[4,6,15] Comparing the evaporation effects of SHiCF and PCF-air-laid paper, the water transport capacity of the air-laid paper is particularly important in order to improve the evaporation rate. In addition, the superhydrophilic treatment exploiting the synergistic effect between enhanced light

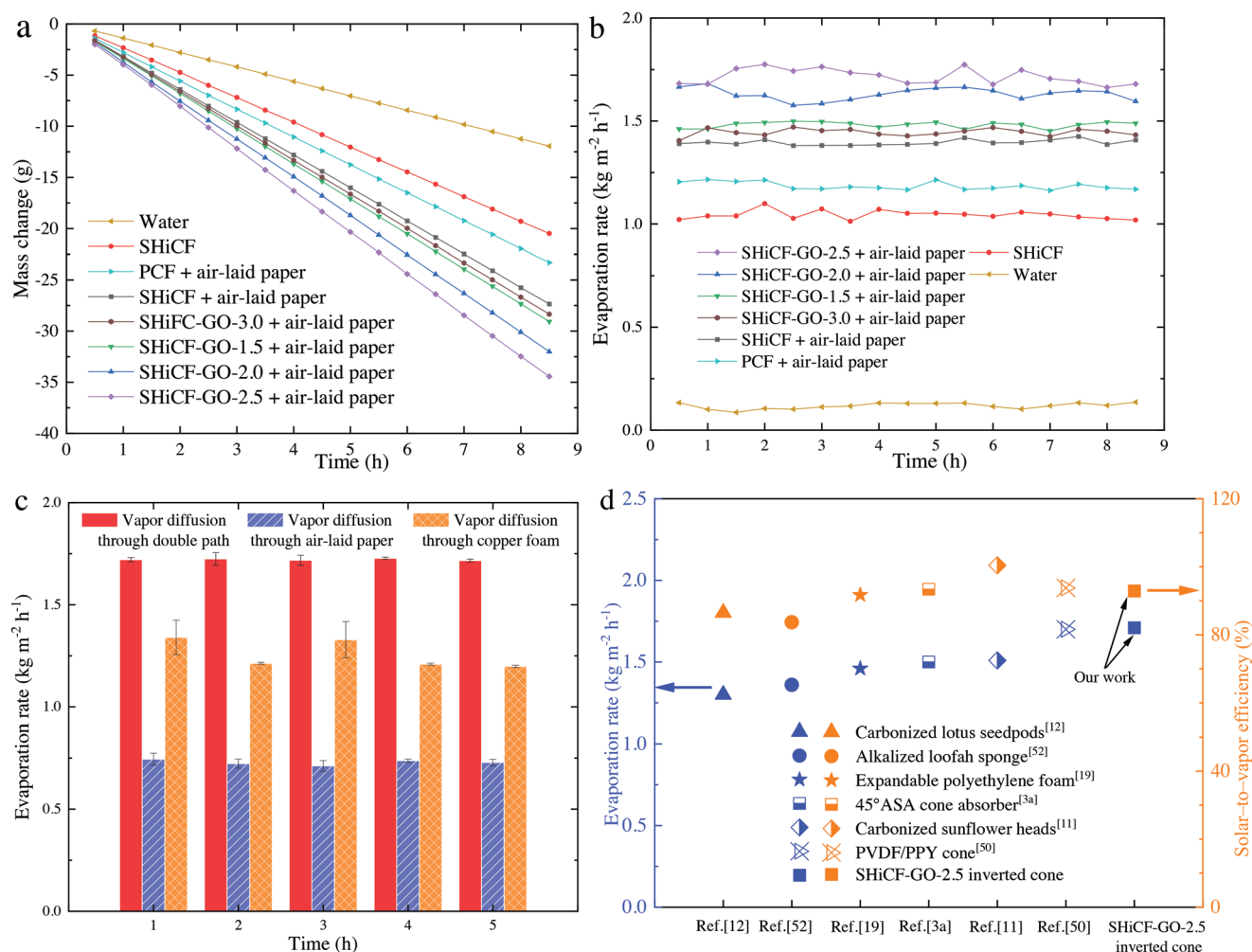


Figure 3. Evaporation performance. a) Mass change (g) of water versus time (h) and b) evaporation rate ($\text{kg}\cdot\text{m}^{-2}\cdot\text{h}^{-1}$) versus time (h) for water, SHiCF, PCF-air-laid paper, SHiCF-air-laid paper, and SHiCF-GO-air-laid paper for different GO concentrations configurations under 1-Sun. c) Evaporation rate for (red) double-layer vapor diffusion path, (blue) air-laid paper vapor diffusion path, and (orange) SHiCF-GO vapor diffusion path. The average and standard deviation have been obtained from three independent measurements. d) Evaporation rates ($\text{kg}\cdot\text{m}^{-2}\cdot\text{h}^{-1}$) and solar-to-vapor efficiency (%) reported in this work in blue and orange respectively, and those reported in the literature for carbonized lotus seedpods,^[12] alkalized loofah sponge,^[52] expandable polyethylene foam,^[19] 45° ASA cone absorber,^[3a] carbonized sunflower heads,^[11] and PVDF/PPY cone.^[50]

absorption and wicking liquid transport offers larger evaporation rates and higher efficiencies than for those cases tested independently. However, the evaporation rate of the conical air-laid paper is only measured to be $0.60 \text{ kg}\cdot\text{m}^{-2}\cdot\text{h}^{-1}$, which indicates that the evaporation rate cannot be prominently improved without the presence of the CF. This is demonstrated by the twofold evaporation rate on the PCF-air-laid paper when compared to the air-laid paper alone. Despite the poor water transport enabled by the PCF, the low evaporation rate reported on the air-laid paper is mainly owed to the white and smooth surface of the air-laid paper that weakens sunlight absorption. The strong water absorption of the air-laid paper coupled to the outstanding light capture ability of the micro- and/or nano-structures of the SHiCF and the high thermal conductivity of the CF, provides excellent evaporation rates nearly 20% higher than that for the PCF-air-laid paper configuration.

While the synergistic cooperation of SHiCF and air-laid paper demonstrates higher evaporation rates when compared

to these operating independently, these rates are still below the maximum production rates reported in this work. In order to improve the light absorption as well as the water transport in both liquid and vapor phases, the influence of GO concentration on evaporation is investigated. The SHiCF is then immersed into a GO-water solution at four different concentrations of 1.5, 2.0, 2.5, and 3.0 mg mL^{-1} rendering the SHiCF-GO-1.5, SHiCF-GO-2.0, SHiCF-GO-2.5, and SHiCF-GO-3.0 samples. The evaporation rates obtained are 1.48, 1.59, 1.71, and 1.46 $\text{kg}\cdot\text{m}^{-2}\cdot\text{h}^{-1}$, respectively, as reported in Figure 3b. The maximum evaporation rate for the SHiCF-GO-2.5 is found as $1.71 \text{ kg}\cdot\text{m}^{-2}\cdot\text{h}^{-1}$, while the net evaporation rate calculated as the difference in evaporation rates between solar light and dark environments is $1.62 \text{ kg}\cdot\text{m}^{-2}\cdot\text{h}^{-1}$. Experiments of evaporation in dark environment at room temperature yielded greater evaporation rates for SHiCF-GO-2.5 of $0.09 \text{ kg}\cdot\text{m}^{-2}\cdot\text{h}^{-1}$ when compared to those for pure water of $0.06 \text{ kg}\cdot\text{m}^{-2}\cdot\text{h}^{-1}$, which is a 50% enhancement. The evaporation rates enhancement in dark environment in

the presence of the SHiCF-GO-2.5 conical evaporator is solely due to enhanced water/air interfacial area empowered by the SHiCF-GO-2.5 conical evaporator when compared to absence of the 3D functionalized structure. For GO concentration lower than 2.5 mg mL^{-1} , an obvious trend where higher water evaporation rate is obtained with the increase of GO concentration is observed. Higher GO concentration leads to an increase in the number of electrons that can transition internally and absorb light, which in turn increases the amount of photons absorbed^[49] and the water sorption capabilities.^[23] Nonetheless, for concentrations higher than 2.5 mg mL^{-1} , evaporation rate decreases presumably as a consequence of the accumulation of GO impregnated within the superhydrophilic skeleton, reducing surface roughness and blocking the pores of the CF, which was shown in Figure 1f, ultimately hindering both liquid and vapor water transport as well as light adsorption. Aiming to quantitatively compare our results with those of other authors, SHiCF-GO-2.5 yields the highest evaporation rate of $1.71 \text{ kg} \cdot \text{m}^{-2} \cdot \text{h}^{-1}$, which is significantly higher than the evaporation rates for deionized water reported for a 3D conical Janus evaporator with an apex angle of 45° reported by Cao et al.^[3a] of $1.50 \text{ kg} \cdot \text{m}^{-2} \cdot \text{h}^{-1}$; and a higher solar-to-vapor efficiency of 93% with respect to 91% reported in Cao et al. Specific details on the evaporation rate calculations can be found in Supporting Information. All efficiencies are calculated by subtracting the evaporation rate in dark environments.^[3a] Evaporation rate and solar thermal evaporation efficiency are in very close agreement with the values reported in the work of Wang et al.^[50] nonetheless, we report on an easier and scalable fabrication procedure via wet oxidation and wet impregnation followed by drying at ambient temperature without the requirement for a chamber, vacuum pump, cold trap, furnace and the different carrier and precursor gases typically used during Chemical Vapor Deposition Polymerization process. When looking into other works, 30% greater evaporation rates are reported when compared to the work of Yu et al. in the absence of airflow or convection.^[51] Compared to recently reported volumetric solar-vapor generation systems, the evaporation performance of the here reported 3D conical CF evaporator shows the best performance in terms of evaporation rate under 1-Sun when compared to other reported configurations in the literature as shown in Figure 3d and also in Table S3 and Figure S9, Supporting Information. When looking into Figure 3d, SHiCF-GO-2.5 yields the highest evaporation rates amongst the cone evaporation rates reported recently with evaporation rates within 1 to 1.3 times greater than that of other cone evaporators,^[11,12,19,50,52] and is 14% higher than that of 45° ASA cone evaporators at the same cone angle.^[3a] While the evaporation efficiency of the inverted cone evaporation system is 7% higher than that of the carbonized lotus seedpods with the same inner cavity structure,^[12] and is at the same level of $\approx 92\text{--}94\%$ with expandable polyethylene foam, PVDF/PPY cone, and 45° ASA.^[3a,19,50] To note is the lower solar-to-vapor efficiency of the SHiCF-GO-2.5 when compared to carbonized sunflower heads while SHiCF-GO-2.5 is able to maintain 10% greater evaporation rates than carbonized sunflower heads.^[11] The evaporation rates are maximized by exploiting efficient water transport along the interface and effective vapor diffusion through the pores ensuring a proper balance between water supply and evaporation at the interface

rather than having water within the pores of the evaporator hindering vapor diffusion as compared to carbon fiber, ASA, or cup shape evaporators.^[3a,10,43] In addition, to minimize heat loss, which in turn helps to maximize water vapor generation, in this work we make use of an air-laid paper and a polyethylene foam so to insulate the evaporator from the bulk water as well as preventing the pores from being filled with excess water when compared to earlier reported evaporators with inner cavity structures.^[50,53] Although out of the scope of this communication, SHiCF-GO-2.5 was found to maintain its mechanical properties and physical appearance even after 7 days of continuous operation as shown in Figure S11, Supporting Information, which is owed to the interconnected small pore-size structure resulting in a very small amount of salt accumulation at the end of water transport. Moreover, SHiCF showed no degradation in the evaporation rates even after 2 days of continuous solar evaporation operation in seawater with salinity of 15 wt.%, as shown in Figure S12, Supporting Information.

2.4. Solar Evaporator Heat Transfer Performance

In order to understand the mechanism of solar thermal evaporation enhancement empowered by the synergistic cooperation of the 3D conical shape, SHiCF, air-laid paper, and GO, and for the different configurations sketched in Figure 4e, the temperature variations under 1-Sun illumination are monitored during the experiment. Specific details on the location of the thermocouple and the procedure for acquiring the different temperatures can be further found in the accompanying Supporting Information. In the case of SHiCF-GO configuration in steady state, the evaporator temperatures are evenly distributed along the system under no energy input, while temperatures increase differently with water having the lowest temperature as represented in Figure 4a. Further schematics including the complete 9 temperature distributions in time along the solar evaporator under 1-Sun for all configurations studied, which support steady state, are further found in Figure S7, Supporting Information for bulk water (Figure S7a,b, Supporting Information), SHiCF + air-laid paper (Figure S7c,d, Supporting Information), air-laid paper (Figure S7e,f, Supporting Information), PCF + air-laid paper at (Figure S7g,h, Supporting Information), SHiCF at 1-Sun (Figure S7i,j, Supporting Information), and SHiCF-GO-2.5 + air-laid paper under 1-Sun illumination (Figure S7k,l, Supporting Information).

On one hand, the temperature variations of bulk water in the absence of a 3D inverted cone solar evaporator under 1-Sun at steady state raised from 18.8 to 31.1°C as shown in Figure 4b as the bulk water absorbs all the heat from the light source. Despite the expected evaporative cooling effect, the temperature of the bulk water is the highest in this case. On the other hand, when the 3D inverted cone evaporator is directly exposed to sunlight, the temperature in the upper part of the inner surface of the cone is slightly the highest since it is closest to the light source (Figure 4c,d). The heat converted from the solar energy radiation depends on the photothermal effect of the evaporator. Thereafter the heat is conducted from the inner surface of the SHiCF-GO toward the outer surface along the wall thickness of the evaporator and toward the air-laid paper.

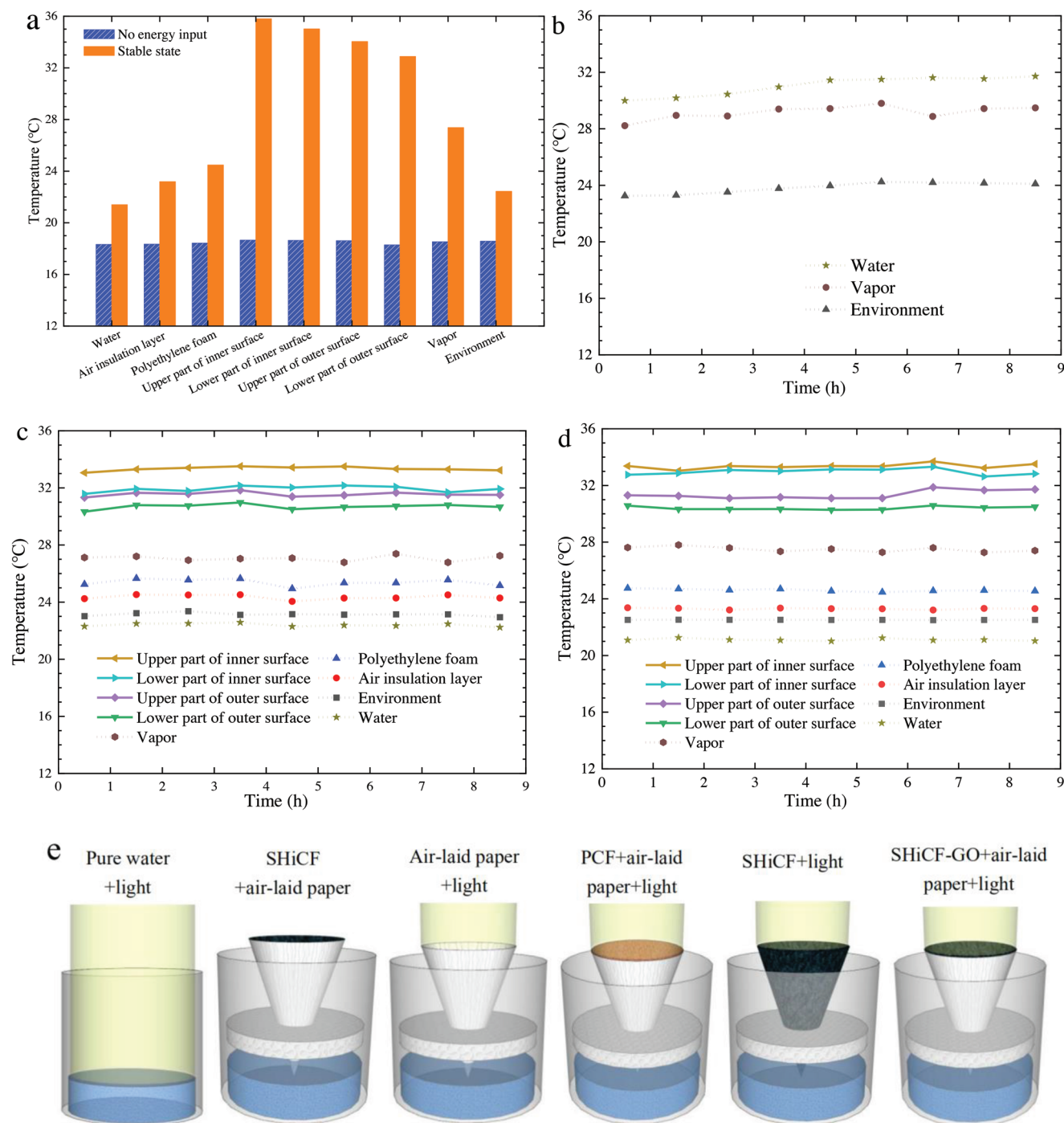


Figure 4. Photothermal conversion capability of the solar evaporator under 1-Sun. Temperature (°C) of each structural layer of solar evaporator a) before energy input and c,d) after system stability. b–d) The temperature (°C) distribution in time (h) for b) pure water, c) SHiCF evaporator, and d) SHiCF-GO evaporator under 1-Sun. e) Schematics of the different configurations studied including pure water, SHiCF, and SHiCF-GO solar evaporator for the temperatures distributions in (b), (c), and (d).

Such heat transport supports the realization of thermal localization. The heat within the 3D structure of the evaporator is maximized by the presence of an insulation layer limiting the conduction of heat loss from the evaporator to the bulk water. During evaporation, heat is transferred and removed from the inner surface of the evaporator due to water evaporative

cooling, while the heat of conduction in the downward direction and through the SHiCF-GO is negligibly small owed to the insulation layer action. Looking at the temperature differences between the different layers of the polyethylene foam, air insulation, and bulk water, it is worth noting that the insulation layer gradually absorbs the excess of heat that is not utilized for

evaporation; nonetheless, a small part of the heat is conducted downward to the bulk water. (Figure 4c,d). The implementation of the polyethylene foam and air insulating layers effectively prevents the heat losses by conduction from the 3D evaporator to the bulk water, because of the low thermal conductivities of both the polyethylene foam and air, which are 0.033 and $0.027 \text{ W} \cdot \text{m}^{-1} \cdot \text{K}^{-1}$,^[3a,54] respectively. With the contribution of the foam structure and the insulation layer, the temperature variation of the bulk water is the smallest in steady state conditions for any studied configuration (Figure 4c,d). The temperature difference between the bulk water and the environment is also negligibly small, supporting further that the heat transfer between water and the environment can be neglected. On the contrary, without the help of the air-laid paper, the bottom of the SHiCF-GO would directly come in contact with the bulk water resulting in direct heat transfer from the SHiCF-GO to the bulk water. If the SHiCF-GO were to contact the bulk water directly, the water temperature would actually raise higher than that of the environment with the consequent anticipated heat losses first from the SHiCF-GO to the bulk water and then from the bulk water to the ambient (Figure S7i,j, Supporting Information).

In the presence of the SHiCF-GO-2.5 3D inverted cone solar evaporator (Figure 4d) the bulk water temperature at steady state conditions remains almost constant at $21.4 \text{ }^\circ\text{C}$. The small temperature raise further demonstrates the effectiveness of the insulation by combining polyethylene foam and a layer of air, which eventually reduces the heat of conduction from the evaporator to the bulk water. Whereas when the 3D inverted cone-shaped solar evaporator is composed solely of the air-laid paper and insulation layer, the maximum surface temperature under 1-Sun irradiation reaches $29.1 \text{ }^\circ\text{C}$ (Figure S7e,f, Supporting Information). Upon the implementation of the PCF wrapped with air-laid paper, the maximum surface temperature of the evaporator reaches $32.2 \text{ }^\circ\text{C}$ (Figure S7g,h, Supporting Information). This highlights that high thermal conductivity 3D foam materials are ideal candidates for solar interfacial evaporation as provide excellent solar radiation absorption capacity and high energy utilization efficiency.

Notably, the greater temperature differences along the evaporator are found for SHiCF and for SHiCF-GO-2.5 as represented in Figure 4c,d. In these configurations, the insulating polyethylene foam temperature is kept at $\approx 25 \text{ }^\circ\text{C}$ while the temperatures of the evaporator varied between 30 and $34 \text{ }^\circ\text{C}$. The inner surface temperature difference at different locations, between upper and lower regions, for the case of the SHiCF evaporator is $1.2 \text{ }^\circ\text{C}$ (Figure 4c), and the maximum inner surface temperature at the upper part of the inner surface is maintained approximately constant at $33.3 \text{ }^\circ\text{C}$. The high temperatures observed are caused by the solar radiation from the light source being absorbed by the superhydrophilic micro-/nano-structures. In addition, heated up water molecules at the evaporating interface generate vapor which removes large amounts of heat through the enthalpy of vaporization, that is, evaporative cooling.^[55] The temperature difference between the upper and lower parts of the inner surface of the evaporator is small, which proves there is good heat of conduction along the SHiCF from top to bottom and the heat is efficiently used in evaporating the water. The occurrence of vapor within the pores

of the foam structure may reduce to some extent the effective thermal conductivity of the CF.

Compared to the SHiCF solar evaporator without GO, the SHiCF-GO solar evaporator exhibits enhanced sunlight absorption, which eventually enhances the photothermal conversion ability of the solar evaporator. Upon reaching steady state, the maximum interfacial temperature of the SHiCF-GO solar evaporation reaches $33.7 \text{ }^\circ\text{C}$ as shown in Figure 4d. The temperature of the inner surface is about $1.9 \text{ }^\circ\text{C}$ higher than that of the outer surface. This difference is greater than in the case of the SHiCF and originates from the better absorbance provided by the GO, which heats up the water present within the pores of the SHiCF skeleton. It is worth noting the greater maximum interfacial temperatures for SHiCF-GO-1.5 and SHiCF-GO-2.0 reaching 33.9 and $34.5 \text{ }^\circ\text{C}$ respectively as represented in Figure S7l,m, Supporting Information, which is caused by the lack of water liquid and vapor diffusion and hence the hindered water evaporation and heat removal from the evaporator. With the addition of GO, the evaporator surface temperature rises slightly when compared to the absence of GO, which depends on the enhancement of light absorption capacity coupled to the water and vapor transport through the pores.

As in most heat transfer processes, there are energy inefficiencies associated with the process. On one hand, during photothermal conversion, the surface of the absorber cannot absorb all the light emitted by the light source, while on the other hand, there are heat losses mainly in the form of radiant, convective, and conductive heat losses (Figure 5).^[4]

Although the thermal insulation layers effectively inhibit heat losses and significantly improve the utilization of solar energy, it is still difficult to completely avoid these losses during the experiment and in practical applications. Since the surface temperature of the SHiCF-GO-2.5 solar evaporator is higher

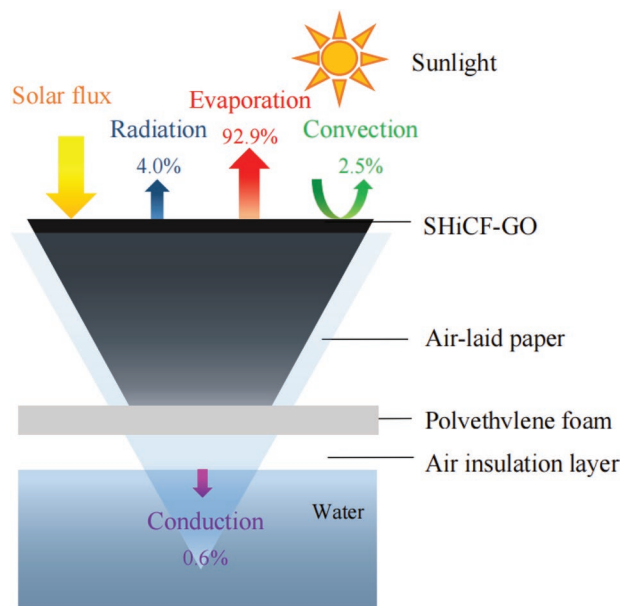


Figure 5. Schematics of the energy balance of the 3D conical SHiCF-GO-2.5 solar evaporator. Energy balance and heat loss diagram of the 3D solar evaporator under 1-Sun illumination.

than absolute zero, there is always inevitable thermal radiation estimated as 4.0% of the total heat converted from the incident light. In addition, there is a temperature difference between the evaporator and the surrounding air, so the heat loss caused by convection should also be considered, although these are minimized by the use of the polyethylene foam and the air insulation layer and estimated as 2.5%. Due to the small thickness of the polyethylene foam, air insulation layer, and air-laid paper, the heat loss by conduction is also the smallest and equals 0.6% for a total measured evaporation efficiency of 93%. The energy balance analysis for the PCF, SHiCF, and SHiCF-GO-2.5 solar evaporators is shown in Table S2, Supporting Information. The heat of conduction losses for the PCF, SHiCF, and SHiCF-GO-2.5 decrease significantly from 2.0% to 1.0% and 0.6%, respectively, which is mainly owed to the more even temperature distribution along the SHiCF-GO skeleton as well as the slight raise in the bulk water temperature. Due to the relatively high surface temperature, the radiant heat loss of the SHiCF evaporator is slightly higher. However, after adding the GO coating, the incident light power of the evaporator is significantly increased and the energy losses by the reflected light are hence meaningfully reduced, so that the evaporation efficiency of the PCF, SHiCF, and SHiCF-GO increases from 68% to 85% and to 93%, respectively.

3. Conclusions

We report a 3D inverted conical solar evaporator supported by a micro-/nano-structured CF skeleton further decorated with graphene oxide, which realizes efficient and stable solar-driven interfacial evaporation by heat localization. The hierarchical porous features of the SHiCF functionalized with graphene oxide, that is, SHiCF-GO, empowers superior synergistic regulation of water and vapor transport via diffusion minimizing heat transfer losses and maximizing the heat transfer from the incident solar light as well as evaporation rates. Evaporation rates are as high as $1.71 \text{ kg} \cdot \text{m}^{-2} \cdot \text{h}^{-1}$ with evaporation efficiency of 93% under 1-Sun illumination. The achieved ultrahigh solar energy harvesting is empowered by the dense pores in the evaporator and the micro- and/or nano-structures covering the surface that reached high sunlight absorption efficiency by the multiple reflections of incident light. Compared with conventional solar evaporators, the 3D structure here presented enables additional sunlight reflection within the main cavity while the presence of the superhydrophilic micro-/nano-structures CF skeleton and graphene oxide functionalization empower both high liquid water transport, high thermal conductivity, and unimpeded water vapor diffusion through the pores. All these qualities anticipate high interfacial water evaporation ideal for the design and optimization of solar evaporators. The utilization of metal foam to expand the evaporation interface to the micro level is also highlighted. Featuring the maximization of broadband solar absorption, continuous water transport, optimization of the evaporation process, and minimization of heat loss, the high efficiency of the 3D inverted cone solar evaporator features as a potential candidate for enabling efficient freshwater extraction from earth-abundant seawater.

4. Experimental Section

Fabrication Procedure: The 3D (three-dimensional) inverted conical solar evaporator with a cone's apex angle of 45° provides an enhanced projected area for the light incidence while maintaining a reasonable height for the water transport toward the top of the cone.^[3a] The other relevant dimensions of the cone were the mouth diameter of 55.0 mm, bottom mouth 8.0 mm, and wall thickness of 2.0 mm. Sketch of the solar evaporator principle and that of the 3D inverted conical solar evaporator configuration studied in this work are represented in Figure 1a,b. The skeleton of the conical evaporator was fabricated using 130 PPI (Pores Per Linear Inch) copper foam (CF) with a porosity of 96.5% (Figure S1a, Supporting Information). The reader is reminded that the pristine copper foam (PCF) was soft and fluffy and can be easily bent and folded into the desired conical shape. This creates the relevant 3D structured network where the inner microscale pores act as optical traps (Figure S1b, Supporting Information) allowing the repeated absorption of a large amount of reflected light experiencing multiple diffuse reflections along the cone matrix as well as enabling liquid water transport.^[27] Chemical oxidation in alkaline solution treatment was then adopted to create a uniform layer of copper oxide nano-blade-like superhydrophilic (SHi) nanostructures decorating the skeleton surface of the CF as well as modifying its chemical and physical properties,^[26] henceforth referred to as SHiCF, which etching procedure is exemplified in Figure 1c.

First, the PCF was cleaned in a $\approx 2\text{--}5 \text{ wt}\%$ hydrochloric acid (HCl) solution to remove any oxide layer on the CF skeleton. After being rinsed with deionized water, the CF was immersed into the mixture solution of sodium hydroxide NaOH ($2.5 \text{ mol} \cdot \text{L}^{-1}$) and ammonium persulfate $(\text{NH}_4)_2\text{S}_2\text{O}_8$ ($0.1 \text{ mol} \cdot \text{L}^{-1}$) at 70°C for 30 min to form the superhydrophilic hierarchical micro- and/or nano- structures on the skeleton of the inverted CF cone, i.e., SHiCF (Figure 1c).^[56] Then it was washed again with plenty of deionized water and dried at room temperature until completely dehydrated. Afterward, the prepared SHiCF inverted cone was immersed into a GO-water solution at different concentrations ranging from 1.5 to $3.0 \text{ mg} \cdot \text{mL}^{-1}$ (at intervals of $0.5 \text{ mg} \cdot \text{mL}^{-1}$). Finally, after being placed at room temperature for 12 h, a black SHiCF inverted cone decorated with GO (SHiCF-GO) was obtained (Figure S3c, Supporting Information). The same procedure in the absence of GO impregnation was also adopted to fabricate the SHiCF for comparison.

An SEM ZEISS Ultra Plus (Germany) was utilized to observe the microstructure of the porous materials. Snapshots of the multi aperture structure of SHiCF shows the unique skeleton structure with pores and the effect of GO impregnation in the pores as represented in Figure 1def. In order to compare the effect of light absorption of plane samples, the absorption rates of PCF, SHiCF, and SHiCF-GO samples were measured using an ultraviolet-visible-near infrared (UV-VIS-NIR) spectrophotometer Shimadzu UV-3600 (Japan). The functional groups of the SHiCF and SHiCF-GO were measured by Fourier Transform Infrared (FTIR) spectroscopy in a Nicolet iN10 MX (America). To prove the existence of the different types of water molecules, Raman spectra of water confined within the SHiCF and the SHiCF-GO were measured using a spectrometer Renishaw inVia Qontor (United Kingdom).

Solar Evaporation Apparatus: In order to obtain the energy utilization efficiency of the 3D conical evaporator for solar evaporation, experiments were conducted to compare the evaporation rate and heat transfer performance of the solar evaporator. In order to quantitatively analyze the heat transfer performance, a total of 9 thermocouples connected to a data acquisition instrument Keysight DAQ970A (America) with an accuracy of $\pm 0.5^\circ\text{C}$ and in turn connected to a PC (Figure S6a,b, Supporting Information) were utilized. More details on the specific location of the thermocouple as well as the procedure followed for acquiring the different temperatures can be further found in the accompanying Supporting Information. Solar thermal phase-change evaporation experiments and measurements of the evaporation rate were carried out by placing the complete solar evaporator apparatus sketched in Figure 1b on an electronic scale Shimadzu AUW120D (Japan) with an accuracy of $\pm 0.0001 \text{ g}$ so to record the mass change of the bulk water under 1-Sun irradiation in time. A Xenon Lamp System CEL-S500 (China)

light source was utilized to simulate the 1-Sun irradiation. Comparing the evaporation rate of the pure water in the absence of the designed evaporator, that is, plain polyethylene foam, with the experimental data from others confirms the accuracy and repeatability of solar heat flux of the light source.^[3a,4,10]

To further enhance the transport path supplying water to the evaporator, an air-laid paper of 0.3 mm in thickness was cut into a fan-shape and wrapped around the conical CF (Figure S1b,c, Supporting Information). When the lower part of the air-laid paper was immersed in bulk water, its adhesion to the outer side surface of the CF was further strengthened through strong capillary force. The conical evaporator wrapped with the air-laid paper was then inserted into a concentric circle-shape polystyrene foam, which was placed at a distance of 20.0 mm from the bulk water surface level to prevent conduction heat loss from the evaporator to the bulk water. Water cannot be directly absorbed by the SHiCF from the bulk water because of the existence of the air insulation layer with a thickness of 20.0 mm, which has the same function as the polystyrene foam. The bulk water was contained within a 62 mm diameter and 21 mm thickness for a total volume of 65.0 mL. The air-laid paper was actually required to enable the water transport from the bulk water to the SHiCF skeleton via the capillary effect also minimizing heat transfer from the evaporator to the bulk as per its low thermal conductivity.

Wettability and Capillary Raising Characterization: In order to measure the wettability of the PCF, SHiCF, and SHiCF-GO, square samples with dimensions of 10 mm × 10 mm were prepared by adopting the fabrication method introduced above. Samples were then subjected to a custom-built contact angle goniometry equipped with a CCD camera and a backlight sufficient to observe the complete spreading of a droplet on the different CF configurations. In addition, the permeability of the PCF, SHiCF, and SHiCF-GO was evaluated via capillary rise characterization experiments conducted on the different surfaces. In the capillary rise experiments, first the air-laid paper and porous CF were cut into rectangular samples with a length of 120 mm and a width of 10 mm. Second, samples were hung at a distance of 35 mm above the petri dish at an inclination angle of 67.5° with respect to the horizontal, that is, the same angle as the one adopted by the cone with respect to the horizon. Third, water was slowly injected into the petri dish through a syringe until the water level reaches just below the bottom of the CF test sample.

Supporting Information

Supporting Information is available from the Wiley Online Library or from the author.

Acknowledgements

J.H. acknowledges the support from the National Natural Science Foundation of China under contract no. 22078196 and the Natural Science Foundation of Shanghai under contract no. 22ZR1460400. F. Y. L. acknowledges the support from the Natural Science Foundation of Shanghai under contract no. 19ZR1401700 and the Talent Introduction Start-up Foundation for Shanghai Institute of Technology under contract no. YJ2020-12. D.O. additionally acknowledges the support from the International Institute for Carbon-Neutral Energy Research (WPI-I2CNER) sponsored by the Japanese Ministry of Education, Culture, Sports, Science, and Technology (MEXT): <https://www.mext.go.jp/en/>, The Royal Society Research Grant 2020 Round 2 with reference RGS/R2/202041, and the European Space Agency (ESA) through the project Convection and Interfacial Mass Exchange (EVAPORATION) with ESA contract number 4000129506/20/NL/PG.

Conflict of Interest

The authors declare no conflict of interest.

Author Contributions

F. Y. L. contributed to conceptualization, methodology, writing, reviewing, and editing, and designed the experimental setup. J.M. designed the experimental setup, performed the experiment, curated the data, and contributed to writing. J.H. contributed to supervision and suggestions. D.O. contributed to discussions, suggestions, writing, reviewing, and editing.

Data Availability Statement

The data that support the findings of this study are available from the corresponding author upon reasonable request.

Keywords

3D inverted conical solar evaporators, graphene oxide, high-efficiency vapor generation and transport, solar interfacial evaporation, superhydrophilic hierarchical copper foam

Received: January 25, 2023

Revised: March 29, 2023

Published online:

- [1] a) G. Ni, G. Li, S. V. Boriskina, H. Li, W. Yang, T. Zhang, G. Chen, *Nat. Energy* **2016**, *1*, 16126; b) M. J. Kalmutzki, C. S. Diercks, O. M. Yaghi, *Adv. Mater.* **2018**, *30*, 1704304.
- [2] C. Zhang, H. Q. Liang, Z. K. Xu, Z. Wang, *Adv. Sci.* **2019**, *6*, 1900883.
- [3] a) N. Cao, S. Lu, R. Yao, C. Liu, Q. Xiong, W. Qin, X. Wu, *Chem. Eng. J.* **2020**, *397*, 125522; b) L. Zhu, M. Gao, C. K. N. Peh, G. W. Ho, *Nano Energy* **2019**, *57*, 507.
- [4] C. Tian, J. Liu, R. Ruan, X. Tian, X. Lai, L. Xing, Y. Su, W. Huang, Y. Cao, J. Tu, *Small* **2020**, *16*, 2000573.
- [5] D. N. Thoai, Q. T. Hoai Ta, T. T. Truong, H. Van Nam, G. Van Vo, *J. Cleaner Prod.* **2021**, *293*, 126122.
- [6] a) J. Lei, Y. Tian, D. Zhou, W. Ye, Y. Huang, Y. Zhang, *Sol. Energy* **2021**, *221*, 75; b) H. Ghasemi, G. Ni, A. M. Marconnet, J. Loomis, S. Yerci, N. Miljkovic, G. Chen, *Nat. Commun.* **2014**, *5*, 4449.
- [7] a) Z. Yu, S. Cheng, C. Li, L. Li, J. Yang, *ACS Appl. Mater. Interfaces* **2019**, *11*, 32038; b) Z. Deng, J. Zhou, L. Miao, C. Liu, Y. Peng, L. Sun, S. Tanemura, *J. Mater. Chem. A* **2017**, *5*, 7691.
- [8] X. Li, G. Ni, T. Cooper, N. Xu, J. Li, L. Zhou, X. Hu, B. Zhu, P. Yao, *J. Zhu, Joule* **2019**, *3*, 1798.
- [9] a) X. Li, J. Li, J. Lu, N. Xu, C. Chen, X. Min, B. Zhu, H. Li, L. Zhou, S. Zhu, T. Zhang, J. Zhu, *Joule* **2018**, *2*, 1331; b) J. Wang, Y. Li, L. Deng, N. Wei, Y. Weng, S. Dong, D. Qi, J. Qiu, X. Chen, T. Wu, *Adv. Mater.* **2017**, *29*, 1603730; c) L. Zhou, Y. Tan, J. Wang, W. Xu, Y. Yuan, W. Cai, S. Zhu, J. Zhu, *Nat. Photonics* **2016**, *10*, 393.
- [10] Y. Shi, R. Li, Y. Jin, S. Zhuo, L. Shi, J. Chang, S. Hong, K.-C. Ng, *J. Wang, Joule* **2018**, *2*, 1171.
- [11] P. Sun, W. Zhang, I. Zada, Y. Zhang, J. Gu, Q. Liu, H. Su, D. Pantelic, B. Jelenkovic, D. Zhang, *ACS Appl. Mater. Interfaces* **2020**, *12*, 2171.
- [12] J. Fang, J. Liu, J. Gu, Q. Liu, W. Zhang, H. Su, D. Zhang, *Chem. Mater.* **2018**, *30*, 6217.
- [13] Y. Li, H. Chen, S. Xiao, M. A. Alibakhshi, C. W. Lo, M. C. Lu, C. Duan, *ACS Nano* **2019**, *13*, 3363.
- [14] H. Zhang, X. Shen, E. Kim, M. Wang, J. H. Lee, H. Chen, G. Zhang, J. K. Kim, *Adv. Funct. Mater.* **2022**, *32*, 2111794.
- [15] X. Zhang, T. Zhang, X. An, M. Li, D. Pei, J. Zhang, C. Li, *Chem. Eng. J.* **2022**, *428*, 131178.

- [16] Y. Yang, X. Yang, L. Fu, M. Zou, A. Cao, Y. Du, Q. Yuan, C.-H. Yan, *ACS Energy Lett.* **2018**, *3*, 1165.
- [17] Y. Wang, X. Wu, T. Gao, Y. Lu, X. Yang, G. Y. Chen, G. Owens, H. Xu, *Nano Energy* **2021**, *79*, 105477.
- [18] L. Zhang, X. Li, Y. Zhong, A. Leroy, Z. Xu, L. Zhao, E. N. Wang, *Nat. Commun.* **2022**, *13*, 849.
- [19] X. Wang, Q. Gan, R. Chen, H. Peng, T. Zhang, M. Ye, *ACS Sustainable Chem. Eng.* **2020**, *8*, 7753.
- [20] J. Chen, B. Li, G. Hu, R. Aleisa, S. Lei, F. Yang, D. Liu, F. Lyu, M. Wang, X. Ge, F. Qian, Q. Zhang, Y. Yin, *Nano Lett.* **2020**, *20*, 6051.
- [21] Y. Fu, G. Wang, X. Ming, X. Liu, B. Hou, T. Mei, J. Li, J. Wang, X. Wang, *Carbon* **2018**, *130*, 250.
- [22] G. Ni, N. Miljkovic, H. Ghasemi, X. Huang, S. V. Boriskina, C.-T. Lin, J. Wang, Y. Xu, M. M. Rahman, T. Zhang, G. Chen, *Nano Energy* **2015**, *17*, 290.
- [23] P. Zhang, J. Li, L. Lv, Y. Zhao, L. Qu, *ACS Nano* **2017**, *11*, 5087.
- [24] S. Wang, Y. Fan, F. Wang, Y. Su, X. Zhou, Z. Zhu, H. Sun, W. Liang, A. Li, *Desalination* **2021**, *505*, 114982.
- [25] D. J. Preston, K. L. Wilke, Z. Lu, S. S. Cruz, Y. Zhao, L. L. Becerra, E. N. Wang, *Langmuir* **2018**, *34*, 4658.
- [26] S. H. Girei, M. M. Alkhabet, Y. M. Kamil, H. N. Lim, M. A. Mahdi, M. H. Yaacob, *Sensors* **2021**, *21*, 020556.
- [27] L. Su, Y. Hu, Z. Ma, L. Miao, J. Zhou, Y. Ning, Z. Chang, B. Wu, M. Cao, R. Xia, J. Qian, *Sol. Energy Mater. Sol. Cells* **2020**, *210*, 110484.
- [28] P. Zhang, Y. Maeda, F. Lv, Y. Takata, D. Orejon, *ACS Appl. Mater. Interfaces* **2017**, *9*, 35391.
- [29] J. Yang, Y. Pang, W. Huang, S. K. Shaw, J. Schiffbauer, M. A. Pillers, X. Mu, S. Luo, T. Zhang, Y. Huang, G. Li, S. Ptasinska, M. Lieberman, T. Luo, *ACS Nano* **2017**, *11*, 5510.
- [30] a) X. Yan, Z. Huang, S. Sett, J. Oh, H. Cha, L. Li, L. Feng, Y. Wu, C. Zhao, D. Orejon, F. Chen, N. Miljkovic, *ACS Nano* **2019**, *13*, 4160; b) A. Sinha, P. Ranjan, A. D. Thakur, *Appl. Phys. A* **2021**, *127*, 127585; c) F. Zhao, L. Wang, Y. Zhao, L. Qu, L. Dai, *Adv. Mater.* **2017**, *29*, 1604927; d) G. Wang, Y. Fu, A. Guo, T. Mei, J. Wang, J. Li, X. Wang, *Chem. Mater.* **2017**, *29*, 5629.
- [31] M. Hosseini, J. Azamat, H. Erfan-Niya, *Appl. Surf. Sci.* **2018**, *427*, 1000.
- [32] a) S. Takahama, G. Ruggeri, A. M. Dillner, *Atmos. Meas. Tech.* **2016**, *9*, 3429; b) E. K. Palupi, P. H. Nazopatul, R. Umam, B. Bibin Andriana, H. Sato, H. Alatas, Irzaman, *IOP Conf. Ser.: Earth Environ. Sci.* **2020**, *460*, 012030; c) E. Fumoto, S. Sato, T. Takanohashi, *Energy Fuels* **2020**, *34*, 5231.
- [33] a) W. Zhou, C. Zhou, C. Deng, L. Chen, X. Zeng, Y. Zhang, L. Tan, B. Hu, S. Guo, L. Dong, S. C. Tan, *Adv. Funct. Mater.* **2022**, *32*, 2113264; b) F. Zhao, X. Zhou, Y. Shi, X. Qian, M. Alexander, X. Zhao, S. Mendez, R. Yang, L. Qu, G. Yu, *Nat. Nanotechnol.* **2018**, *13*, 489; c) L. Li, N. He, B. Jiang, K. Yu, Q. Zhang, H. Zhang, D. Tang, Y. Song, *Adv. Funct. Mater.* **2021**, *31*, 2104380.
- [34] H. Wang, R. Zhang, D. Yuan, S. Xu, L. Wang, *Adv. Funct. Mater.* **2020**, *30*, 2003995.
- [35] a) K. K. Liu, Q. Jiang, S. Tadepalli, R. Raliya, P. Biswas, R. R. Naik, S. Singamaneni, *ACS Appl. Mater. Interfaces* **2017**, *9*, 7675; b) M. S. Zielinski, J. W. Choi, T. L. Grange, M. Modestino, S. M. Hashemi, Y. Pu, S. Birkhold, J. A. Hubbell, D. Psaltis, *Nano Lett.* **2016**, *16*, 2159.
- [36] H. Jiang, L. Ai, M. Chen, J. Jiang, *ACS Sustainable Chem. Eng.* **2020**, *8*, 10833.
- [37] Z. Hong, J. Pei, Y. Wang, B. Cao, M. Mao, H. Liu, H. Jiang, Q. An, X. Liu, X. Hu, *Energy Convers. Manage.* **2019**, *199*, 112019.
- [38] W. Li, C. Lin, G. Huang, J. Hur, B. Huang, S. Yao, *Adv. Sci.* **2022**, *9*, 2201738.
- [39] Y. Li, T. Gao, Z. Yang, C. Chen, Y. Kuang, J. Song, C. Jia, E. M. Hitz, B. Yang, L. Hu, *Nano Energy* **2017**, *41*, 201.
- [40] F. Nasehnia, S. Mohammadpour Lima, M. Seifi, E. Mehran, *Comput. Mater. Sci.* **2016**, *114*, 112.
- [41] C. Jia, Y. Li, Z. Yang, G. Chen, Y. Yao, F. Jiang, Y. Kuang, G. Pastel, H. Xie, B. Yang, S. Das, L. Hu, *Joule* **2017**, *1*, 588.
- [42] a) C. Chang, P. Tao, B. Fu, J. Xu, C. Song, J. Wu, W. Shang, T. Deng, *ACS Omega* **2019**, *4*, 3546; b) Y. Liu, S. Yu, R. Feng, A. Bernard, Y. Liu, Y. Zhang, H. Duan, W. Shang, P. Tao, C. Song, T. Deng, *Adv. Mater.* **2015**, *27*, 2768.
- [43] Y. Bu, Y. Zhou, W. Lei, L. Ren, J. Xiao, H. Yang, W. Xu, J. Li, *J. Mater. Chem. A* **2022**, *10*, 2856.
- [44] M. R. S. Shirazy, L. G. Fréchette, *Int. J. Heat Mass Transfer* **2013**, *58*, 282.
- [45] N. Fries, M. Dreyer, *J. Colloid Interface Sci.* **2008**, *320*, 259.
- [46] A. Guo, X. Ming, Y. Fu, G. Wang, X. Wang, *ACS Appl. Mater. Interfaces* **2017**, *9*, 29958.
- [47] Z. Wang, X. Wu, F. He, S. Peng, Y. Li, *Adv. Funct. Mater.* **2021**, *31*, 201114.
- [48] Y. S. Jun, X. Wu, D. Ghim, Q. Jiang, S. Cao, S. Singamaneni, *Acc. Chem. Res.* **2019**, *52*, 1215.
- [49] A. Johansson, H.-C. Tsai, J. Aumanen, J. Koivistoinen, P. Myllyperkiö, Y.-Z. Hung, M.-C. Chuang, C.-H. Chen, W. Y. Woon, M. Pettersson, *Carbon* **2017**, *115*, 77.
- [50] Y. Wang, C. Wang, X. Song, M. Huang, S. K. Megarajan, S. F. Shaukat, H. Jiang, *J. Mater. Chem. A* **2018**, *6*, 9874.
- [51] Y. Guo, X. Zhou, F. Zhao, J. Bae, B. Rosenberger, G. Yu, *ACS Nano* **2019**, *13*, 7913.
- [52] Y. Lu, X. Wang, D. Fan, H. Yang, H. Xu, H. Min, X. Yang, *Sustainable Mater. Technol.* **2020**, *25*, e00180.
- [53] a) W. Li, Z. Li, K. Bertelsmann, D. E. Fan, *Adv. Mater.* **2019**, *31*, 1900720; b) B. Bai, X. Yang, R. Tian, W. Ren, R. Suo, H. Wang, *Appl. Therm. Eng.* **2019**, *163*, 114379.
- [54] T. L. Bergman, F. P. Incropera, D. P. DeWitt, A. S. Lavine, *Fundamentals of Heat and Mass Transfer*, 8th Edition, Wiley, New York, USA, **2018**.
- [55] X. Wu, Y. Wang, P. Wu, J. Zhao, Y. Lu, X. Yang, H. Xu, *Adv. Funct. Mater.* **2021**, *31*, 2102618.
- [56] P. Zhang, F. Y. Lv, A. Askounis, D. Orejon, B. Shen, *Int. J. Heat Mass Transfer* **2017**, *109*, 1229.